Head-mounted adaptive optics visual simulator

Shoaib R. Soomro,[1,2] **Santiago Sager,**[1,3] **Alba M. Paniagua-Diaz,**[3] **Pedro M. Prieto,**[3] **and Pablo Artal**[3,*]

[1]*Voptica S.L., Campus de Espinardo (Edificio Pleiades), 30100 Murcia, Spain*
[2]*Electronic Engineering Department, Mehran University of Engineering and Technology, Pakistan*
[3]*Laboratorio de Óptica, Universidad de Murcia, Campus de Espinardo (Edificio 34), 30100 Murcia, Spain*
[*]*pablo@um.es*

Abstract: Adaptive optics visual simulation is a powerful tool for vision testing and evaluation. However, the existing instruments either have fixed tabletop configurations or, being wearable, only offer the correction of defocus. This paper proposes a novel head-mounted adaptive optics visual simulator that can measure and modify complex ocular aberrations in real-time. The prototype is composed of two optical modules, one for the objective assessment of aberrations and the second for wavefront modulation, all of which are integrated into a wearable headset. The device incorporates a microdisplay for stimulus generation, a liquid crystal on silicon (LCoS) spatial light modulator for wavefront manipulation, and a Hartmann-Shack wavefront sensor. Miniature optical components and optical path folding structures, together with in-house 3D printed mounts and housing, were adapted to realize the compact size. The system was calibrated by characterizing and compensating the internal aberrations of the visual relay. The performance of the prototype was analyzed by evaluating the measurement and compensation of low-order and higher-order aberrations induced through trial lenses and phase masks in an artificial eye. The defocus curves for a simulated bifocal diffractive lens were evaluated in real eyes. The results show high accuracy while measuring and compensating for the induced defocus, astigmatism, and higher-order aberrations, whereas the MTF analysis shows post-correction resolution of up to 37.5 cycles/degree (VA 1.25). Moreover, the subjective test results show the defocus curves closely matched to a commercial desktop visual simulator.

1. Introduction

Human vision is a sensory system that includes both optics of the eye and neural information processing. Although each step of vision perception—starting from light transfer through the eye's optics to the interpretation of the scene by the brain—is equally important, the first physical limit on the perceived visual quality is imposed by the optics of the eye. The optical aberrations degrade the quality of the image formed on the retina. Ocular aberrations, including defocus and astigmatism (i.e., sphero-cylindrical refraction), are among the leading causes of vision problems in the world [1]. On the other hand, there are circumstances where a controlled amount of aberrations can lead to better visual performance, for example by increasing the depth of focus for presbyopic subjects [2].

Visual simulation is an emerging and promising method that allows the measurement and manipulation of optical aberrations by employing the principles of adaptive optics (AO) [3]. The AO visual simulators incorporate wavefront sensors and wavefront manipulators to measure aberrations and perform subjective testing to evaluate the relation between optical and visual quality [4,5]. The stimulus wavefront is manipulated to induce or compensate for the aberrations, to evaluate their impact on perceived visual quality. Although initially intended and explored for military and astronomical applications, the AO technologies have been effectively used in vision science to better understand the characteristics of the eye [3,4,6], and have secured an important place for clinical applications. The wavefront-guided and topography-guided

correction of refraction has allowed customized laser ablation profiles for patients minimizing the effects of higher-order aberrations (HOA). Visual simulation through AO has enabled a better understanding of the benefits and consequences of the HOA and simulate post-operative vision through intraocular-lens (IOL) before cataract surgeries. The AO has also supported the understanding of the effects of neural adaptation and perceptual learning in specific groups of the population such as patients suffering from myopia, keratoconus, and presbyopia.

Below is an overview of the existing AO visual simulators followed by the proposed head-mounted AO instrument that can address some of the important concerns.

The early demonstrations of the AO visual simulator date back more than two decades. The first-generation systems incorporated membrane deformable mirrors (DM) for wavefront manipulation and were built on optical tables in laboratory settings [7,8]. The system allowed the generation of different wavefronts. However, large amounts of aberrations could not be induced due to the limited deformation range of the membrane mirrors [9]. The later works replaced the deformable mirrors with programable LCoS spatial light modulators (LCoS-SLM) which brought flexibility in terms of stroke and mode independence [10,11]. The LCoS-SLMs allow the induction/compensation of wide-range defocus, astigmatism, coma, and other high-order aberrations with better control of the incident wavefront. However, the main drawback of LCoS-SLMs over DMs is light efficiency. While the DMs are highly reflective and can offer up to 99% reflectivity, LCoS-SLMs involve the use of polarizers and have a transmissive layer that absorbs a part of light during modulation. Accordingly, LCoS-based systems require brighter stimuli generators. Another potential drawback of LCos-SLMs over continuous surface DMs is their segmented architecture and their limited stroke, usually around 1 wavelength, while DMs can produce several wavelengths of peak-to-valley. However, the very lack of continuity constraints in LCoS-SLMs can be exploited to increase their effective stroke by operating them in 2π-wrapping mode (i.e., modulus 1-wavelength), while the very high resolution of current LCoS chips minimizes the undesired effects of wavefront segmentation. In fact, due to the independent pixel-level phase control, the LCoS-SLMs can also simulate multifocal lenses and diffractive optical elements, as reported in previous works [12], which is unfeasible with continuous DMs. Both DM- and LCoS-SLM-based AO visual simulators have been broadly used to understand the different visual properties. Piers *et al.* used the AO visual simulator to determine the optimum value of the ocular spherical aberration [13]. Artal *et al.* studied the magnitude and causes of night myopia with an AO simulator [14]. Mu *et al.* explored the aberration corrections in the model eye using an LCoS-SLM-based AO system [15]. Legras *et al.* reported the benefit of correcting HOA using a 52-point magnetically actuated DM-based adaptive optics system [16]. Elliott *et al.* explored the use of a DM-based close-loop adaptive optics system to test the visual benefit of compensating monochromatic HOA [17]. Hampson *et al.* studied the effects of aberration dynamics on the control of static accommodation using a 37-actuator piezoelectric deformable mirror combined with a Hartmann-Shack (HS) sensor [18,19]. Another study used a DM-based AO system to correct eccentric refractive errors and HOA in the presence of long-standing central scotoma [20]. Dai *et al.* reported the combination of an AO visual simulation system with perpetual learning and modifying control matrix and superposition of aberrations in real-time [21]. Venkataraman *et al.* studied the resolution and contrast sensitivity in peripheral vision in the presence of monochromatic and chromatic aberrations induced through an AO visual simulator [22]. Jiang *et al.* explored the compensation of longitudinal chromatic aberrations using an AO vision simulation system [23]. Similarly, the LCoS-SLM-based AO system has also been used to simulate the visual outcome of multifocal intraocular lenses [12]. Further developments extended the AO visual simulator concept to binocular configuration to enable simultaneous testing and visual evaluation of both eyes [24]. The binocular AO simulators have been explored to study stereopsis in aberrated eyes [25], binocular visual acuity (VA) in the presence of monochromatic and polychromatic light [26], and the impact of HOA correction

on binocular VA [27]. A clinical AO visual simulator was also developed and commercialized in the form of a tabletop instrument that can perform various types of visual tests [28,29]. The recent developments included the addition of a focus tunable lens to increase the correction range of the instrument for highly myopic subjects [30,31] and the use of vertically aligned low-cost LCoS-SLM modulators for wavefront manipulation and higher order aberrations in subjects [32,33].

On the other hand, the development of portable and wearable instruments has been mostly focused on the use of tunable lenses [34–38]. A wearable device has been demonstrated for multifocal correction through the temporal multiplexing of a tunable lens [34,35]. Smart spectacles for presbyopia correction have been proposed by synchronizing real-time pupil and gaze tracking with tunable lenses [36,37]. Similarly, the solid-state LIDAR camera and the liquid membrane-based tunable lens-based vision correction spectacles have also been demonstrated to evaluate presbyopia [38]. Recently, holographic display techniques have also been explored to simulate vision correction and perform a preoperative visual evaluation for cataract surgeries [39,40].

The above-mentioned techniques and systems have demonstrated the great potential of AO for visual simulation. However, their wide-scale implementation has been mainly limited due to two important factors: The tabletop AO visual simulators offer wavefront sensing and aberration correction features on a single platform. However, such instruments are only useful in fixed clinical settings due to their bulkiness and sophisticated handling requirements. On the other hand, the tunable lens-based instruments offer portability and compactness suitable for the wearable form factor. However, such instruments can only simulate the correction of focal power and do not perform objective measurements.

Here we present a novel head-mounted AO visual simulator for objective and subjective visual evaluation. The proposed instrument offers a wearable form factor in a headset format that can perform aberration corrections and carry out wavefront sensing simultaneously. Compared to the existing AO simulators, which are either tabletop and bulky or offer limited objective and subjective testing using separate devices, the proposed system integrates the wavefront sensing and wavefront manipulation mechanisms on a single wearable headset and is capable of evaluating the complex aberrations, including HOA. The proposed instrument offers the much-needed integration and mobility to allow large-scale implementations and wider reach to locations with limited eye-care facilities. The wearable form factor and compact size also introduce the AO technology to optometrists and ophthalmologists in an easy-to-use configuration. The fundamental concept of the proposed instrument is inspired by the tabletop AO visual simulator (the VAO Simulator) developed by Voptica S.L. (Murcia, Spain) [28]. The visual correction is facilitated by incorporating a liquid crystal on a silicon spatial light modulator (LCoS-SLM) while the aberration measurement is performed using the HS sensor. The folded optical layout and customized device assembly ensure the smaller instrument footprints suitable for wearable configurations.

2. Methods

2.1. Optical layout

The system design consists of two optical units: (1) a visual manipulation module, and (2) an aberration measurement module. Figure 1(a) shows the simplified optical layout of the system. Both modules are integrated into a single layout suitable for the wearable assembly. To ensure the compact size and precise positioning of the optical elements, the optical design was simulated and optimized in a ray tracing software (Ansys Zemax OpticsStudio 14, USA). Figure 1(b) shows the optical design of the instrument. The visual module consists of a stimuli screen (i.e., micro-display), achromatic lenses L_1-L_5, folding mirrors M_1-M_3, and the LCoS-SLM. Light from the stimuli screen is collimated through L_1 and passed through a circular aperture to define

the system pupil. A relay telescope with unit magnification is then employed to image the pupil on the LCoS-SLM. A set of mirrors (M_1 to M_3) is incorporated to fold the optical path. The aberration correction profile is presented on the LCoS-SLM panel conjugated to the incident pupil. The modified pupil reflected from the LCoS-SLM is then transferred to the exit pupil (eye pupil) through a similar relay telescope. A field-stop and linear polarizer are also incorporated to filter the ambient light and the diffractive periodic artifacts that may be produced by the pixelated structure of the LCoS-SLM panel and to minimize the ghost image produced by the non-phase-modulated component of the LCoS-SLM.
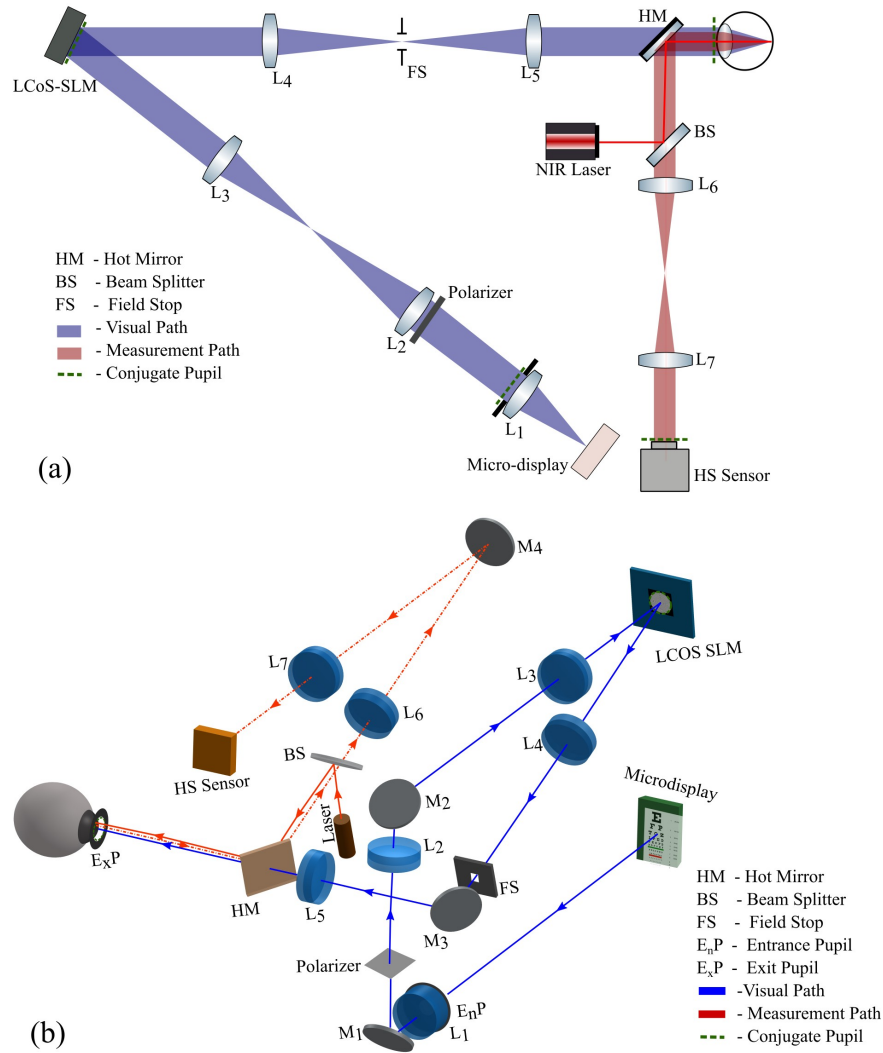
Fig. 1. (a) Simplified optical layout of the adaptive optics visual simulator, (b) The optical design of the proposed head-mounted AO visual simulator. The blue and red ray colors show the visual and measurement channels respectively.

The measurement module consists of a compact near-infrared (NIR) laser, a beam splitter, a pair of NIR-coated achromatic lenses L_6-L_7, a folding mirror M_4, and a customized HS sensor. A narrow-collimated laser beam illuminates the eye and produces a point/dot on the retina. The reflected light is transferred to the HS sensor via a relay telescope. A pupil de-magnification

factor of 0.5 is maintained in the relay telescope to ensure the fitting of the imaged pupil on the sensor area. Moreover, a hot mirror is used before the exit pupil to separate the visual and measurement channels.

2.2.   Experimental prototype

The prototype instrument was developed based on the optical layout shown in Fig. 1(b). It uses a high-definition micro-display (SYL2271, Syndiant Inc, USA) to act as a stimuli screen. The micro-display uses a sequential color reflective intensity modulator, beam splitter, and an RGB backlight LED, and has a 6.4 µm pixel pitch and 0.37″ diagonal size which provided 1280×720 pixels resolution. A 125 mm focal length visible achromatic doublet lens (No. 69-922, Edmund Optics, UK) is used to collimate the stimuli image that offers a $3.71° \times 2.1°$ field-of-view with an angular resolution of 10 arcseconds. A fixed-size aperture of 4 mm diameter is used as the entrance pupil of the system.

A pair of 50 mm focal-length visible achromatic doublet lenses (No. 47-667, Edmund Optics, UK) is used to relay the pupil towards the LCoS-SLM with unit magnification. A pair of silver-coated mirrors (No. PF05-03-P01, Thorlabs, USA) attached to miniaturized kinematic mounts (MK05/M, Thorlabs, USA) are employed to fold the optical path. Our wavefront manipulator is a phase-only LCoS-SLM (PLUTO-2-VIS-014, Holoeye Photonics AG, Berlin, Germany). The LCoS-SLM has full HD resolution (1920×1080 squared pixels of 8 µm size) with 0.7″ diagonal panel size and 93% fill factor. The LCoS-SLM has a parallel-aligned nematic liquid crystal layer sandwiched between a transparent electrode and a silicon wafer with an etched array of pixels. The phase modulation is achieved by transferring the 8-bit grayscale images to the LCoS panel via a multimedia interface. The gray-level value of each pixel induces the corresponding phase retardation to the incoming wavefront. The phase retardation of LCoS-SLM was linearized through a calibration procedure as reported in [41]. The linearization ensures the phase retardation in the range of 0-2π for 0-255 grayscale values at 532 nm wavelength. The different RGB wavelengths in microdisplay introduce small changes in the phase retardation ranges. However, the effect is small [42] and no noticeable chromatic artifacts were observed during visual corrections which is also evident in the figures shown in the results section. The manipulated wavefront is then relayed to the eye using a similar telescopic arrangement consisting of an achromatic lens pair of 50 mm focal length (No. 47-667, Edmund Optics, UK), and a silver-coated mirror (No. PF05-03-P01, Thorlabs, USA). The linear polarizer film (LPVISE2X2, Thorlabs, USA) was placed close to the entrance pupil while a custom-made rectangular slit of size 3.5×2 mm², 3D printed using Polylactic acid (PLA) material, was used as a field-stop.

The measurement relay consists of a compact NIR laser module (Thorlabs, CPS780S) emitting at 780 nm wavelength. A small aperture of about 1 mm diameter was placed in front of the laser beam to produce a point-like image on the retina and act as a reference beacon for wavefront sensing. Moreover, a neutral density (ND) filter (NDUV505A, Thorlabs, USA) is used to attenuate laser power below 50 µW. The 780 nm wavelength laser produces a very small visible dot on the retina which only covers a very small portion (less than 0.2 degrees) of the visual field. However, to avoid patient discomfort, the laser is interfaced and controlled through the system software and is only activated during objective measurement. The laser remains off during the rest of the testing procedure to avoid potential interference with the perceived stimulus image. The eye's pupil is optically conjugated to the HS sensor using a relay telescope that consisted of NIR-coated doublet lenses of 100 mm and 50 mm focal length (No. 49-333, Edmund Optics UK, and AC127-050-B, Thorlabs, USA), and a fold mirror (No. PF05-03-P01, Thorlabs, USA). The NIR beam splitter (No. 48-391, Edmund Optics, UK) was used to introduce the Ariel pointing laser in the measurement relay, and a hot mirror (No. 62-628, Edmund Optics, UK) was used to separate the visual and measurement channels.

Our custom-made HS sensor is comprised of an off-the-shelf microlens array with a 3.17 mm focal length and 192 µm pitch (APO-Q-P192-F3.17, Flexible Optical B.V., Rijswijk, Netherlands) and a 3.1-megapixel CMOS sensor (DMM 37UX252-ML, The Imaging Source Europe GmbH, Germany).

The optomechanical assembly of the instrument was based on the customized housing and mounts as shown in Fig. 2. The housing assembly was designed in the 3D CAD tool (Solidworks, Dassault Systèmes, France) and manufactured in-house with acrylonitrile butadiene styrene (ABS) material using a fused deposition modeling (FDM) 3D printer. The housings consist of two separate base parts for visual and measurement modules that are fixed on a sandwiched part. A pair of 3D-printed covers were used to enclose the optical components and the driver printed circuit boards of the LCoS-SLM and the microdisplay. Finally, an eye-piece part attached to an off-the-shelf headband was incorporated to align and attach the instrument to the subject's head. Figure 3 shows the finished prototype instrument tethered to a computer. The micro-display and the LCoS-SLM are interfaced through a high-definition multimedia interface (HDMI) while the HS sensor and IR laser were connected and powered via an USB interface. The instrument was operated through dedicated software developed in C++.
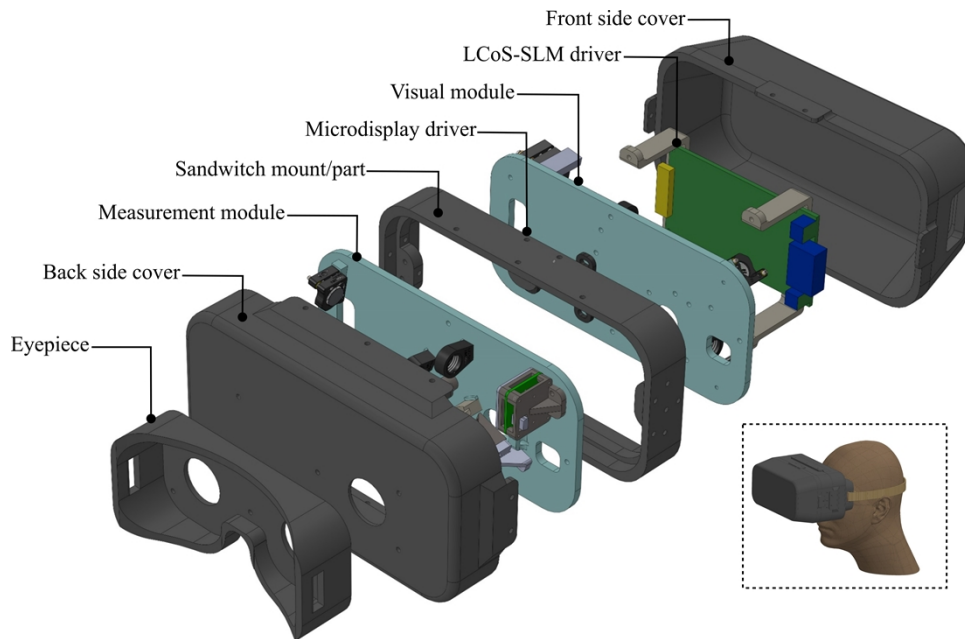
Fig. 2. Customized housing assembly showing different parts of the instrument and their arrangement. The housing parts are custom-designed using 3D CAD tools and printed in-house on a fused deposition modeling (FDM) 3D printer.
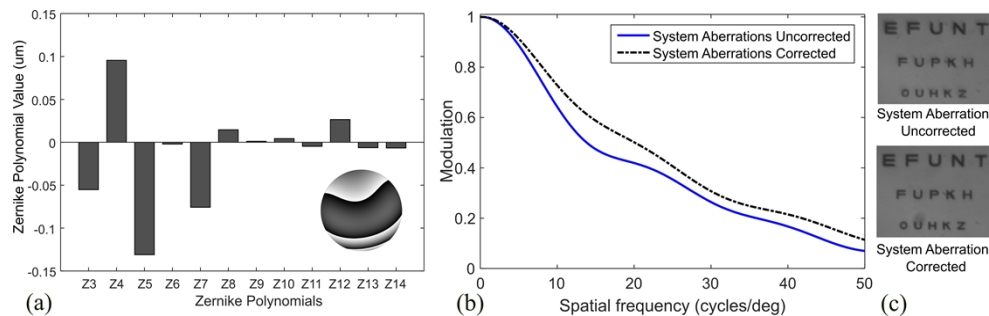
2.3. Compensation for the system's aberrations

The prototype instrument uses miniature optical components with short focal length lenses which may introduce aberrations and affect the reference visual quality. To avoid that, a calibration step was performed to characterize and compensate for the internal aberrations of the system. We used a collimated beam of 532 nm laser diode, introduced at the entrance pupil, and an external HS wavefront sensor at the exit pupil of the system. The laser beam followed the visual relay path and was recorded by the HS wavefront sensor to determine the Zernike polynomial coefficients. Figure 4(a) shows the measurement results in OSA/ANSI Zernike polynomial ordering standard:
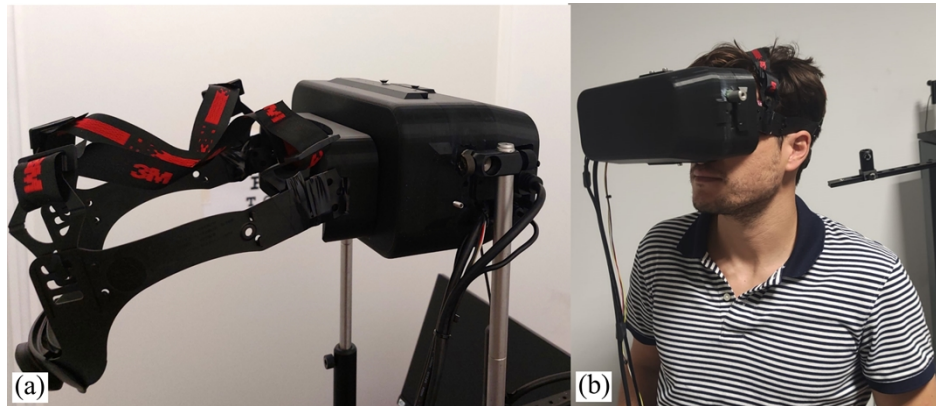
Fig. 3. (a) Experimental prototype of the instrument, (b) Subject being tested with the system.

a small value of low-order aberrations including 0.3 D astigmatism, -0.075 μm of vertical coma and 0.026 μm of spherical aberration over a 4 mm diameter pupil. The presence of these minor aberrations is attributed to the slight mismatch of the distance between lenses and conjugate pupil planes and the quality of the doublet lenses.

Fig. 4. (a) Zernike polynomial values for the internal aberrations of the system represented in accordance with OSA/ANSI standard, (b) MTF curves before and after compensation of system aberration, and (c) comparison of visual acuity charts before and after compensation.

The system's aberrations were compensated by introducing its corresponding correction wavefront (as shown in Fig. 4(a) inset) at the LCoS-SLM and analyzing the Modulation Transfer Function (MTF) to compare the pre-calibration and post-calibration visual quality. We used the slanted edge MTF determination techniques to experimentally measure the MTF profile [43]. In short, the stimuli screen displayed the image of a slanted edge which was recorded by an auxiliary camera positioned at the exit pupil of the system. The edge profiles, before and after compensation, were captured on the camera, an oversampled line spread function (LSF) was measured, and the MTF was then determined by evaluating the Fourier transform of the LSF.

The MTF curves indicate a noticeable improvement in visual quality after the correction of the system's internal aberrations as shown in Fig. 4(b). The MTF analysis showed that the uncorrected visual quality of the instrument is significantly high (up to VA 1.25). The visual quality is further enhanced with the compensation of internal aberrations leading to an average MTF improvement of about 20% while around 19% modulation increase is observed at the 30 cycles/degree (VA 1). Figure 4(c) shows the visual acuity charts before and after the compensation

of the system aberrations, confirming a visual quality improvement in line with the MTF results. The visual acuity chart shows the stimuli letters of three different sizes corresponding to VA 0.7, 1, and 1.25, respectively. The comparison of both chart images also indicates that the instrument can be used to show VA 1.25 visual stimuli even without compensation for internal aberrations.

3. Results

3.1. Objective evaluation of aberrations

The wavefront sensing performance of the prototype instrument was tested by measuring the known aberrations in an artificial eye. We used a custom-built model artificial eye consisting of a one-inch achromatic lens of 30 mm focal length (AC254-030-AB, Thorlabs, USA), a 3D printed matt finished flat retina made of PLA material, and a speckle-reducing vibrator (Garosa flat coin button mini vibration motor 1020) enclosed in a 3D printed assembly. The artificial eye was placed at the exit pupil of the system and the aberrations were induced by positioning the trial lenses and HOA-inscribed phase masks in front of the eye pupil. The eye was illuminated with the internal NIR laser and its scattered reflections were captured by the HS wavefront sensor of the instrument. We used a set of spherical and cylindrical trial lenses with optical power ranging from -7 D to +7 D and -4 D to +4 D, respectively, to evaluate the low-order aberrations (LOA) measurement capability of the instrument. A very small difference between measured and induced defocus was found, where the linear fitting of the data points yielded the slope value close to ideal (-1.03) and the coefficient of determination, R^2, greater than 0.999. Moreover, the assessment of the cylindrical trial lenses also showed a similar trend where the linear fitting of the experimental data showed a close fitting to the unity slope value (-1.04) while the determination coefficient, R^2, value was also higher than 0.999.
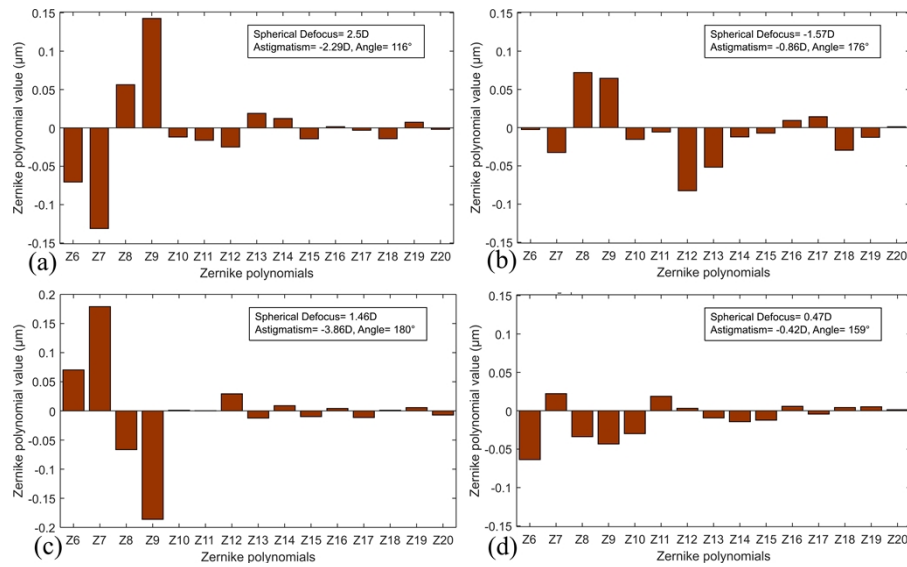
A set of four different phase masks, each representing a different combination of aberrations, were incorporated to assess the HOA measurement feature of the instrument. The phase masks are the segments of Alvarez lenses (Adlens View Plus, Adlens, UK). The Alvarez lenses contained two individual lenses for each eye that move with respect to each other to change the defocus. We used the pieces of those individual lenses as phase masks which induced noticeable HOA as well as defocus and astigmatism depending on the aperture position of the lens. Similar to the previous arrangement, the phase masks were positioned in front of the artificial eye. Each phase mask introduced a significant amount of aberrations of different orders, which are represented in Fig. 5 with their Zernike polynomial values. The phase masks, shown in Fig. 5(a) and Fig. 5(c), induced a noticeable amount of coma and trefoil. The phase mask shown in Fig. 5(b) introduced a combination of coma, trefoil, spherical aberration, and secondary astigmatism in the order of 0.05 μm. The fourth phase mask in Fig. 5(d) had relatively small Zernike polynomial values where vertical trefoil was dominant with 0.06 μm Zernike value.

3.2. Characteristics of simulated vision correction

The performance of the developed prototype for simulating vision corrections was tested by manipulating the aberrated wavefront and evaluating the post-correction quality. Once the induced aberrations were successfully measured, as detailed in Section 3.1, their corresponding wavefront corrections were relayed to the LCoS-SLM. The artificial eye was then replaced with a camera (DMK-72AUC02, Nikon AF Nikkor 28 mm f/2.8) to characterize the quality of the simulated corrections. The process was repeated for spherical and cylindrical defocus trial lenses and HOA phase masks.

Figure 6(a) and Fig. 6(b) respectively show the images of simulated corrections for defocus and astigmatism for different values of optical power. The reference image (0 D) indicates the visual outcome of the calibrated system. The results indicate that the system can effectively undo the induced defocus and astigmatism. Up to VA 1.25 can be achieved for defocus corrections

Fig. 5. Zernike polynomials values in µm represented in the OSA/ANSI ordering format showing the higher-order aberrations induced through four different phase masks and measured with the HS wavefront sensor of the prototype. The text insets in each graph show the LOA for each phase mask.

of up to ±3 D. The results also show that the contrast of the stimuli screen image is degraded after the visual correction, especially for high diopter corrections (i.e. ± 5 D), and the stimuli of higher VA are irresolvable. On the other hand, astigmatism correction in Fig. 6(b) indicates good visual quality (≥ VA 1) for up to ±4 D cylindrical defocus. Similar to defocus lenses, the visual quality of the astigmatism correction is degraded as the optical power of induced/corrected defocus is increased. The loss of contrast is mainly associated with the phase modulation effects of the LCoS-SLM panel. The change of defocus corresponds to a curvature which is translated to the local phase changes on the LCoS-SLM plane, wrapped over 2π. The increase in defocus power corresponds to larger curvature which produces higher phase steps between adjacent LCoS-SLM pixels when the wrapping occurs. The resultant imperfection in modulation due to the discretization of phase change allows most of the light to be modulated correctly. However, part of the unmodulated light produces an uncorrected ghost image (especially for higher defocus) which decreases the contrast.

The MTF analysis of the corrections was also performed to further investigate the effect of wavefront manipulation on different spatial frequencies. MTF evaluation followed the process discussed in Section 2.3. Figure 7(a) and Fig. 7(b) show the MTF curves from -7 D to +7 D defocus and -4 D to +4 D astigmatism corrections, respectively. The reference MTF curve in both graphs shows the best possible MTF, free from external as well as internal aberrations of the system. The results show a degradation in visual performance as the amount of defocus correction is increased which follows the observations in Fig. 6. The maximum loss of visual performance is observed for the -7 D correction, which reaches less than 10% modulation at 16 cycles/degree. The minimum loss of visual outcome is observed for -1 D defocus. On the other hand, the correction to cylindrical lenses shows better visual performance and most of the optical power corrections yield greater than or equal to 10% modulation for spatial frequencies up to 30 cycles/degree. Assuming the 10% MTF as a resolution limit, it can be considered that the prototype instrument allows VA 1 or better for a significant number of the LOA correction values which can also be observed in post-correction VA chart images shown in Fig. 6(a) and Fig. 6(b)
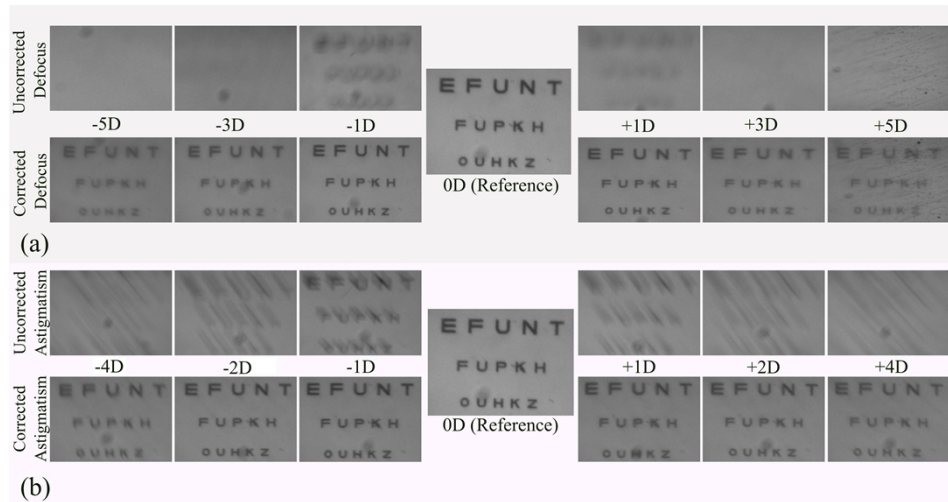
Fig. 6. The results of simulated vision correction for different values of spherical defocus (a), and cylindrical defocus (b). The defocus and astigmatism are induced through trial lenses, measured with the wavefront sensor of the instrument, and corrected via wavefront manipulation. The reference image shows the visual outcome, for VA 0.7, 1, and 1.25, when no external aberrations are induced or corrected.

where the chart letters corresponding of VA 1 (30 cycles/degree) can be resolved. However, it can also be observed that the corrections for -5 D spherical defocus and -3 D cylindrical defocus do not provide enough visual quality to resolve VA 1, which is evident from the blurred letters seen in their respective post-correction chart images, shown in Fig. 6, as well as degraded MTF (less than 10% at 30 cycles/degrees) observed in Fig. 7.
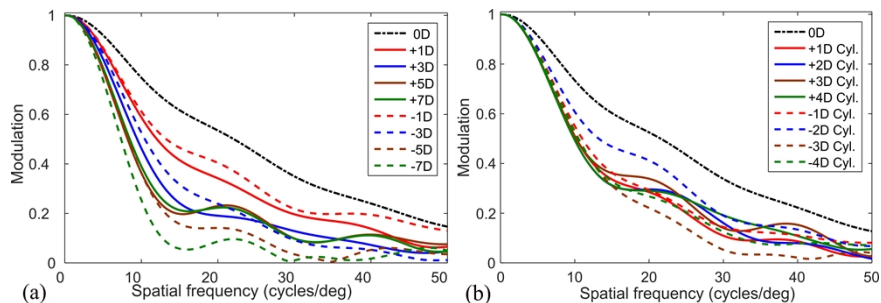
Fig. 7. The post-correction MTF curves of simulated vision corrections for different values of (a) defocus, and (b) astigmatism induced through trial lenses. The analysis shows 10% or better modulation at 30 cycles/degree for the majority of the spherical and cylindrical defocus values. However, some of the corrections, such as -7 and -5 D spherical defocus and -3 D cylindrical defocus, indicate a significant MTF drop, down to 0%, at 30 cycles/degree.

The quality of the HOA correction using the prototype system was evaluated by compensating the aberrations that are induced through HOA phase masks as discussed in Section 3.1. For each phase mask, the correction wavefront was determined based on the measured Zernike polynomial values, as shown in Fig. 5, and was relayed to the LCoS-SLM. The resultant manipulated image was then captured by the camera for further evaluation. Figure 8(a) to Fig. 8(d) shows the results of simulated HOA correction for each phase mask. The MTF curves as well as

acuity chart images indicate a significant improvement in the visual outcome between LOA-only corrections and LOA + HOA corrections. Since the first three-phase masks have higher LOA, their corresponding LOA corrections provide early improvement but do not reach higher visual quality (i.e. VA 1 or higher). However, the subsequent HOA correction further improves visual outcome which is evident from MTF curves as well as acuity chart images. The correction of the phase mask in Fig. 8(d) shows negligible improvement with HOA corrections where the MTF at low spatial frequencies remains the same and only improves for higher spatial frequencies (i.e., > 25 cycles/degree). This is because the specific phase mask has a small LOA and HOA, which can be observed in Fig. 5(d). In summary, it can be generalized that the instrument can effectively characterize and correct HOA and can achieve post-HOA correction acuity better than VA 1 or 30 cycles/degree.
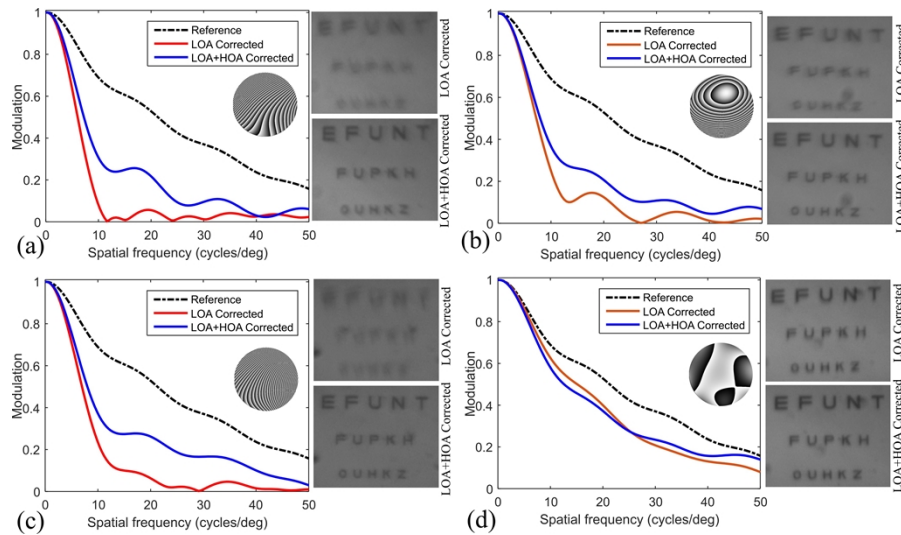
Fig. 8. The post-correction MTF curves and acuity charts of simulated vision correction for four different HOA phase masks (a) to (d). Each graph shows the MTF curves after LOA correction and LOA + HOA correction. The inset wavefront shows the respective correction wavefront phase map relayed to the LCoS-SLM.

3.3. Testing in real eyes

The testing of the developed wearable device in real eyes was performed by simulating a diffractive bifocal lens and evaluating the defocus curve in a pair of subjects. The assessment of the defocus curve allowed relatively simple testing procedures and demonstration of full wavefront manipulation in easily accessible subjects. The selection of participants and execution of testing procedures were in line with the tenets of the Helsinki Declaration and followed the ethical protocols approved by the ethics committee of the University of Murcia.

Our test participants included a presbyopia patient (age 56) and a young subject with paralyzed accommodation (age 29). Each subject underwent a testing procedure that included measurement of through-focus VA on the developed head-mounted device and a commercially available tabletop AO visual simulator (VAO, software version 3.06, firmware 1.01, Voptica S.L.) [28]. The alignment of the subject's eye was done manually with small adjustments while looking for the best vision for the subject. Since only subjective refraction was corrected and the phase profile of the diffractive bifocal lens was symmetrical, the specific position of the pupil was not relevant as long as it was not vignetted by the patient's pupil.

The tests were performed by simulating a diffractive bifocal lens that had an equal energy distribution between two focal powers at 0 D and 3 D, respectively. Three through-focus subjective VA measurements were taken for each of the participants on both devices separately. The subjective refraction of each participant (-1.5 D defocus for S1 and -3.5 D defocus for S2, no astigmatism in both cases) was also determined and used as a baseline. However, no other ocular health checks were performed on both subjects.

The comparison of defocus curves, obtained through both devices, for individual subjects is shown in Fig. 9(a) and Fig. 9(b). While the average defocus curves for both subjects are shown in Fig. 9(c). The results indicate an analogous trend in defocus curves for each subject when tested on both devices. The defocus curves, shown in Fig. 9(a) and Fig. 9 (b), indicate slight variation in the VA of each of the subjects. However, each subject achieves maximum VA close to the focal points of the simulated bifocal lenses, which is evident from the dual peaks observed in each defocus curve. On the other hand, the comparison of average defocus curves, shown in Fig. 9 (c), specifies an equivalent average VA for both devices. Moreover, the standard deviation observed between multiple test trials on both devices was less than 0.25 VA.
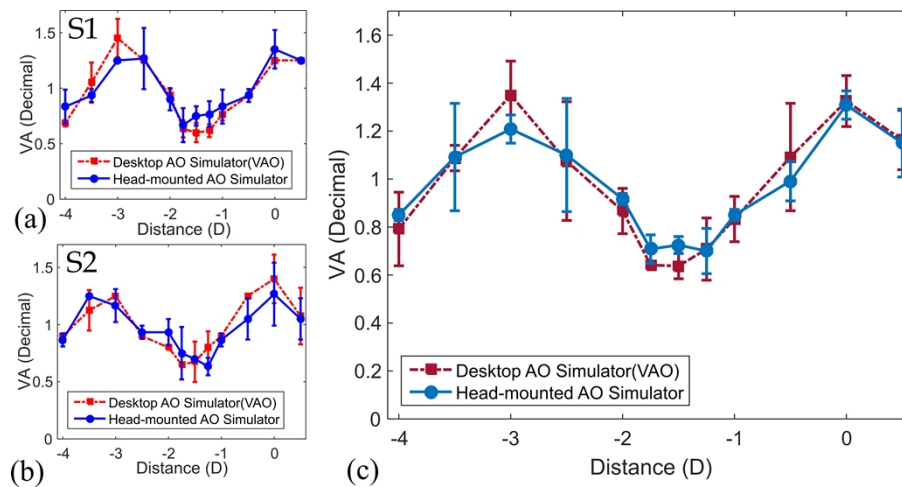
Fig. 9. Subjective evaluation of defocus curves when simulating a diffractive bifocal lens on the developed head-mounted device and commercial desktop AO simulator. (a) shows the comparison of defocus curves for the young subject with paralyzed accommodation, (b) a comparison of defocus curves for the presbyopia patient, and (c) shows the average defocus curves for both subjects. The error bars indicate the standard deviation.

4. Discussion

The instrument presented in this work brings the mobility and wearable form factor to the AO visual simulation technology which is realized through the modified optical design and custom-modeled instrument layout. We designed and built a prototype headset to assess the effectiveness of wavefront sensing and manipulation as an integrated head-mounted platform.

The LCoS-SLM technology is constantly evolving and has been widely explored for AO, holography, and augmented reality. At the current stage, the LCoS-SLMs seem to outperform the other competing technologies (such as deformable mirrors, and tunable lenses) in terms of precise pupil control, high pixel density, and versatile phase modulation [44,45].

The performance of the system for LOA testing was evaluated using trial lenses. The instrument can determine defocus and astigmatism with high accuracy. The linear fitting between induced lens power and measured defocus showed an ideal slope (1.03) with negligible offset (-0.044).

Similarly, the estimated cylindrical axis was within ±5 degrees of the actual lens orientation, which is an insignificant fluctuation from a clinical perspective. Moreover, Fig. 6 and Fig. 7 suggested that the instrument can effectively simulate the defocus and astigmatism correction with high precision enabling post-correction visual testing up to VA 1.25. The accuracy can be further improved through well-defined calibration protocols ensuring improved alignment of lenses and using a more specific set of lenses instead of off-the-shelf standard trial lenses.

An important aspect of an AO visual simulator is its capability to compensate HOA. The HOA correction is highly sensitive to the internal aberrations of the system, requires more precise pupil alignment, and may only be effective for larger pupil sizes [46]. The proposed prototype demonstrates HOA correction by incorporating HOA-inscribed phase masks and a custom-built artificial eye to induce aberrations in controlled settings and minimize alignment errors. The calibration routine to compensate for internal aberrations allows a reduction in wavefront errors during the correction. The HOA correction results indicated an obvious improvement where the post-correction MTF curves, as well as stimuli letters, showed up to 1.25 resolvable VA, which is evidenced in Fig. 8. Several previous works have explored the compensation of HOA in real eyes [27,30,46,47]. Such desktop instruments incorporate patient-specific dental impressions and chinrests for precise pupil alignment. On the other hand, the pupil alignment with our current head-mounted instrument is challenging due to it being mobile and physically attached to the user's head. Moreover, the measurement and correction of HOA in real eyes is only useful when evaluated on specific patients whose visual quality is significantly impacted by HOA rather than LOA. Finding such patients for the subjective study is, both, time-consuming and challenging. Owing to these concerns, the presented experiments demonstrate and evaluate the visual simulations in the artificial eye while the real eye test is performed by evaluating the vision through a simulated diffractive bifocal lens and analyzing its defocus curve. Further optimizations in the size, weight, and design of the headset will allow vision simulation for a broad range of tests in real eyes. Moreover, our current prototype is a monocular system and, therefore does not involve the accommodation-convergence aspect of natural stereoscopic vision. The binocular extension of the proposed head-mounted AO simulator would require additional optical subassembly to facilitate the convergence.

The customized housing of the prototype instrument has been developed keeping in mind the generic design of the typical smart headsets. Previous studies on wearable AO simulators have demonstrated slimmer and lightweight designs by adapting the shape of spectacles. However, they have mainly followed open-view configurations primarily intended to address presbyopia [35–38,48]. Moreover, none of the existing head-mounted AO instruments incorporates LCoS-SLM for visual manipulation. The inclusion of LCoS-SLM offers increased flexibility in terms of wavefront manipulation but requires additional relay optics with multiple lenses and a relatively longer optical path. Additionally, the commercially available LCoS-SLMs come with driver circuit boards of considerable size which must also be integrated into the head-mounted unit. Due to these factors, the developed instrument is larger ($Width \times Height \times Depth = 20 \times 10 \times 15$ cm^3) and heavier (≈ 0.5 kg) than some of the above-mentioned AO spectacles. Refinement in the optical design, inclusion of lightweight 3D printing material, and employing LCoS-SLM with customized application-specific integrated circuits (ASIC) can further reduce the instrument size and weight to bring ergonomic comfort to the users.

5. Conclusions

We propose and demonstrate a new head-mounted AO instrument to measure complex aberrations and simulate their visual corrections to facilitate personalized visual evaluation. The device integrates an HS sensor and an LCoS-SLM-based wavefront manipulation unit in a wearable headset. The miniature optical components and custom-built parts enable a compact instrument size and shape. Internal aberrations of the system were characterized and compensated using an

external laser source and HS wavefront sensor. The AO capability of the system was exhibited by measuring and simulating the LOA and HOA corrections in an artificial eye and simulating the vision through a bifocal diffractive lens in real eyes. The results with HOA phase masks indicate the characterization and compensation of HOA aberrations having noticeable Zernike polynomial values, such as coma, trefoil, spherical aberration, and secondary astigmatism. The aberration corrections demonstrate the post-correction visual quality up to 1.25 VA for defocus and astigmatism corrections of up to ±3 D and ±2 D, respectively. The testing in real eyes indicated defocus curves similar to the ones obtained with a commercial desktop AO visual simulator.

The developed instrument can emerge as the next-generation visual testing tool replacing the bulky instruments in the clinics, allowing mobility and ease of use for optometrists and ophthalmologists, and increasing patient comfort and satisfaction. Future device development focuses on the optimization of optical design and incorporation of custom optical components. Another important future aspect is to demonstrate the real-time HOA measurement and correction in real eyes. Moreover, the integration with high-precision and fast eye-pupil tracking technologies will allow automated pupil alignment and short subjective test time, especially for HOA testing, to augment the clinical implementation of the instrument. On the other hand, further improvements in ergonomic design, the addition of full wireless control, and the extension to accommodation-convergence-supported binocular operation would increase its acceptability, make the proposed instrument a unique platform for visual assessment, and initiate new directions for wearable vision testing tools.

Disclosures. SRS: Voptica S.L. (E, P), SS: Voptica S.L. (E), PP: Voptica S.L. (I, P), PA: Voptica S.L. (I, P)

Data availability. Data underlying the results presented in this paper are not publicly available at this time but may be obtained from the authors upon reasonable request.

References

1. World Health Organization, "Blindness and vision impairment," https://www.who.int/news-room/fact-sheets/detail/blindness-and-visual-impairment.
2. H. Lucía, V. E. A. R. Consuelo, and A. Pablo, "Spherical aberration customization to extend the depth of focus with a clinical adaptive optics visual simulator," J. Refract. Surg. **36**(4), 223–229 (2020).
3. E. Akyol, A. M. Hagag, S. Sivaprasad, *et al.*, "Adaptive optics: principles and applications in ophthalmology," Eye **35**(1), 244–264 (2021).
4. S. Marcos, J. S. Werner, S. A. Burns, *et al.*, "Vision science and adaptive optics, the state of the field," Vision Res. **132**, 3–33 (2017).
5. J. I. W. Morgan, T. Y. P. Chui, and K. Grieve, "Twenty-five years of clinical applications using adaptive optics ophthalmoscopy [Invited]," Biomed. Opt. Express **14**(1), 387 (2023).
6. S. Marcos, P. Artal, D. A. Atchison, *et al.*, "Adaptive optics visual simulators: a review of recent optical designs and applications [Invited]," Biomed. Opt. Express **13**(12), 6508 (2022).
7. E. J. Fernández, S. Manzanera, P. Piers, *et al.*, "Adaptive optics visual simulator," J. Refract. Surg. **18**(5), S634–S638 (2002).
8. E. J. Fernández, I. Iglesias, and P. Artal, "Closed-loop adaptive optics in the human eye," Opt. Lett. **26**(10), 746–748 (2001).
9. E. J. Fernández and P. Artal, "Membrane deformable mirror for adaptive optics: performance limits in visual optics," Opt. Express **11**(9), 1056–1069 (2003).
10. P. M. Prieto, E. J. Fernández, S. Manzanera, *et al.*, "Adaptive optics with a programmable phase modulator: applications in the human eye," Opt. Express **12**(17), 4059–4071 (2004).
11. S. Manzanera, P. M. Prieto, D. B. Ayala, *et al.*, "Liquid crystal Adaptive Optics Visual Simulator: Application to testing and design of ophthalmic optical elements," Opt. Express **15**(24), 16177–16188 (2007).
12. S. Vedhakrishnan, M. Vinas, S. Aissati, *et al.*, "Vision with spatial light modulator simulating multifocal contact lenses in an adaptive optics system," Biomed. Opt. Express **12**(5), 2859 (2021).
13. P. A. Piers, S. Manzanera, P. M. Prieto, *et al.*, "Use of adaptive optics to determine the optimal ocular spherical aberration," J. Cataract Refract. Surg. **33**(10), 1721–1726 (2007).

14. P. Artal, C. Schwarz, C. Cánovas, *et al.*, "Night myopia studied with an adaptive optics visual analyzer," PLoS One **7**(7), e40239 (2012).

15. Q. Mu, Z. Cao, D. Li, *et al.*, "Liquid Crystal based adaptive optics system to compensate both low and high order aberrations in a model eye," Opt. Express **15**(4), 1946–1953 (2007).

16. R. Legras and H. Rouger, "Calculations and measurements of the visual benefit of correcting the higher-order aberrations using adaptive optics technology," J. Optom. **1**(1), 22–29 (2008).

17. S. L. Elliott, S. S. Choi, N. Doble, *et al.*, "Role of high-order aberrations in senescent changes in spatial vision," J. Vis. **9**(2), 24 (2009).

18. K. M. Hampson and E. A. H. Mallen, "Multifractality in steady-state accommodation is robust to dynamic correction of aberrations using adaptive optics," J. Mod. Opt. **59**(12), 1056–1063 (2012).

19. K. M. Hampson, S. Sem Chin, E. A. H Mallen, *et al.*, *Fluctuations in Accommodation: A Review* (Birkhäuser Verlag, 2009), 29(20).

20. K. Baskaran, R. Rosén, P. Lewis, *et al.*, "Benefit of Adaptive Optics Aberration Correction at Preferred Retinal Locus," Optom. Vis. Sci. **89**(9), 1417–1423 (2012).

21. Y. Dai, L. Zhao, F. Xiao, *et al.*, "Adaptive optics vision simulation and perceptual learning system based on a 35-element bimorph deformable mirror," Appl. Opt. **54**(5), 979 (2015).

22. A. P. Venkataraman, P. Papadogiannis, D. Romashchenko, *et al.*, "Peripheral resolution and contrast sensitivity: effects of monochromatic and chromatic aberrations," J. Opt. Soc. Am. A **36**(4), B52 (2019).

23. X. Jiang, J. A. Kuchenbecker, P. Touch, *et al.*, "Measuring and compensating for ocular longitudinal chromatic aberration," Optica **6**(8), 981 (2019).

24. E. J. Fernández, P. M. Prieto, and P. Artal, "Binocular adaptive optics visual simulator," Opt. Lett. **34**(17), 2628–2631 (2009).

25. E. J. Fernández, P. M. Prieto, and P. Artal, "Adaptive optics binocular visual simulator to study stereopsis in the presence of aberrations," J. Opt. Soc. Am. A **27**(11), A48–A55 (2010).

26. C. Schwarz, S. Manzanera, and P. Artal, "Binocular visual performance with aberration correction as a function of light level," J. Vis. **14**(14), 6 (2014).

27. C. Schwarz, P. M. Prieto, E. J. Fernández, *et al.*, "Binocular adaptive optics vision analyzer with full control over the complex pupil functions," Opt. Lett. **36**(24), 4779–4782 (2011).

28. VOPTICA S.L, "VAO Simulator," https://voptica.com/vao/.

29. L. Hervella, E. A. Villegas, P. M. Prieto, *et al.*, "Assessment of subjective refraction with a clinical adaptive optics visual simulator," J. Cataract Refract. Surg. **45**(1), 87–93 (2019).

30. N. Suchkov, E. J. Fernández, and P. Artal, "Wide-range adaptive optics visual simulator with a tunable lens," J. Opt. Soc. Am. A **36**(5), 722 (2019).

31. S. Sager La Ganga, P. M. Prieto, A. M. Paniagua-Diaz, *et al.*, "A compact binocular adaptive optics visual simulator for clinical use in highly-aberrated eyes," Invest. Ophthalmol. Visual Sci. **63**(7), 4548-F0462 (2022).

32. A. Arias, A. M. Paniagua-Diaz, P. M. Prieto, *et al.*, "Phase-only modulation with two vertical aligned liquid crystal devices," Opt. Express **28**(23), 34180 (2020).

33. A. M. Paniagua-Diaz, J. Mompeán, and P. Artal, "Vertical-aligned liquid crystal devices for ocular wavefront correction and simulation," Opt. Eng. **61**(12), 121806 (2022).

34. C. Dorronsoro, A. Radhakrishnan, J. R. Alonso-Sanz, *et al.*, "Portable simultaneous vision device to simulate multifocal corrections," Optica **3**(8), 918 (2016).

35. A. Radhakrishnan, D. Pascual, S. Marcos, *et al.*, "Vision with different presbyopia corrections simulated with a portable binocular visual simulator," PLoS One **14**(8), e0221144 (2019).

36. J. Mompeán, J. L. Aragón, and P. Artal, "Portable device for presbyopia correction with optoelectronic lenses driven by pupil response," Sci. Rep. **10**(1), 20293 (2020).

37. N. Padmanabhan, R. Konrad, and G. Wetzstein, "Autofocals: Gaze-contingent eyeglasses for presbyopes," in *ACM SIGGRAPH 2018 Emerging Technologies, SIGGRAPH 2018* (Association for Computing Machinery, Inc, 2018).

38. R. Agarwala, O. Lukashova Sanz, I. P. Seitz, *et al.*, "Evaluation of a liquid membrane-based tunable lens and a solid-state LIDAR camera feedback system for presbyopia," Biomed. Opt. Express **13**(11), 5849 (2022).

39. D. Kim, S.-W. Nam, K. Bang, *et al.*, "Vision-correcting holographic display: evaluation of aberration correcting hologram," Biomed. Opt. Express **12**(8), 5179 (2021).

40. K. Kavaklı, G. Aydındoğan, E. Ulusoy, *et al.*, "Pupil steering holographic display for pre-operative vision screening of cataracts," Biomed. Opt. Express **12**(12), 7752 (2021).

41. J. L. M. Fuentes, E. J. Fernández, P. M. Prieto, *et al.*, "Interferometric method for phase calibration in liquid crystal spatial light modulators using a self-generated diffraction-grating," Opt. Express **24**(13), 14159 (2016).

42. J. L. Martinez, E. J. Fernandez, P. M. Prieto, *et al.*, "Chromatic aberration control with liquid crystal spatial phase modulators," Opt. Express **25**(9), 9793–9801 (2017).

43. M. Estribeau and P. Magnan, "Fast MTF measurement of CMOS imagers using ISO 12333 slanted-edge methodology," Proc. SPIE **5251**, 243 (2004).

44. E. J. Fernández, P. M. Prieto, and P. Artal, "Wave-aberration control with a liquid crystal on silicon (LCOS) spatial phase modulator," Opt. Express **17**(13), 11013 (2009).

45. Z. Zhang, Z. You, and D. Chu, "Fundamentals of phase-only liquid crystal on silicon (LCOS) devices," Light: Sci. Appl. **3**(10), e213 (2014).

46. D. Williams, G.-Y. Yoon, J. Porter, *et al.*, "Visual Benefit of Correcting Higher Order Aberrations of the Eye [Proceedings of the 1st International Congress on Wavefront Sensing and Aberration-free Refractive Correction]," J. Refract. Surg. **16**(5), S554–S559 (2000).

47. N. Suchkov, E. J. Fernández, and P. Artal, "Impact of longitudinal chromatic aberration on through-focus visual acuity," Opt. Express **27**(24), 35935 (2019).

48. M. U. Karkhanis, A. Banerjee, C. Ghosh, *et al.*, "Compact Models of Presbyopia Accommodative Errors for Wearable Adaptive-Optics Vision Correction Devices," IEEE Access **10**, 68857–68867 (2022).